coatings

MDPI

Article

CMAS Corrosion Behavior of Nanostructured YSZ and Gd-Yb-Y-Stabilized Zirconia Coatings

Lanxin Zou [1,2], Minghao Gao [1], Na Xu [1,*], Jia Zhang [1] and Xinchun Chang [1]

[1] Institute of Metal Research, Chinese Academy of Sciences, Shenyang 110016, China; lxzou21s@imr.ac.cn (L.Z.); mhgao15b@imr.ac.cn (M.G.); jzhang@imr.ac.cn (J.Z.); xcchang@imr.ac.cn (X.C.)
[2] School of Materials Science and Engineering, University of Science and Technology of China, Shenyang 110016, China
* Correspondence: naxu@imr.ac.cn

Abstract: With the development of industry, the operating temperature of aero engines and gas turbines continues to increase; developing thermal barrier coatings (TBCs) with superior resistance to CaO-MgO-Al_2O_3-SiO_2 (CMAS) corrosion has become a prominent research focus. In this study, atmospheric plasma spraying (APS) was used to prepare yttria-stabilized zirconia (YSZ), nanostructured yttria-stabilized zirconia (n-YSZ), and Gd-Yb-Y-stabilized zirconia (GYYSZ) coatings. The effects of CMAS exposure on the microstructure, chemical composition, phase transition, and microhardness of the coatings were investigated. Comparative analysis revealed that both phase transition and exfoliation occurred in corroded YSZ and n-YSZ coatings, with n-YSZ exhibiting more pronounced changes. In contrast, GYYSZ coatings remained stable without phase transition and exhibited a smaller increase in microhardness (270 HV0.3). Consequently, doping Gd/Yb/Y elements into ZrO_2 can improve the performance of TBCs.

Keywords: thermal barrier coatings; CMAS corrosion; atmospheric plasma spraying; nanostructured YSZ; Gd-Yb-Y-stabilized zirconia

Citation: Zou, L.; Gao, M.; Xu, N.; Zhang, J.; Chang, X. CMAS Corrosion Behavior of Nanostructured YSZ and Gd-Yb-Y-Stabilized Zirconia Coatings. *Coatings* **2023**, *13*, 1623. https://doi.org/10.3390/coatings13091623

Academic Editor: Alina Vladescu

Received: 15 August 2023
Revised: 26 August 2023
Accepted: 28 August 2023
Published: 15 September 2023

1. Introduction

Thermal barrier coatings (TBCs) [1,2] are extensively utilized in gas turbines and aero engines to reduce the surface temperature of hot-section components and increase the turbine inlet temperature. The thermal spraying technologies for TBCs mainly include electron beam–physical vapor deposition (EB-PVD) [3] and plasma spraying [1,4]. A typical TBC consists of an 8 wt.% Y_2O_3-stabilized ZrO_2 (8YSZ) ceramic layer [5] and a MCrAlY (M = Ni/Co/Ni + Co) bond coat [6]. However, conventional YSZ TBCs encounter numerous issues above 1200 °C, including oxidation [7,8], phase transition [9], sintering [10], and calcium–magnesium–aluminum-silicate (CMAS) corrosion [11,12]. CMAS is primarily derived from atmospheric dust, runway debris, volcanic ash, and impurities in fuels. In high-temperature service environments, CMAS melts and adheres to the surface of hot-section components as it is ingested into the engine. Subsequently, CMAS infiltrates the pores and microcracks of the coatings, undergoing a series of physical and chemical reactions with the coatings. This process induces a phase transition within the TBCs, culminating in their premature cracking and exfoliation.

To find and develop coatings with improved resistance to CMAS corrosion, research institutes have focused substantial research in the following directions: first, developing novel ceramic coating materials, such as $RE_2Zr_2O_7$ [13–15], $REPO_3$ [16], Ti_2AlC [17], and $Hf_6Ta_2O_{17}$ [18]; second, doping YSZ with oxides, including rare earth oxide-doped YSZ [19,20] and Al- and Ti-doped YSZ [21–23]; third, depositing protective layers on the surface of the coatings, such as the Pt layer [24] and Al_2O_3 layer [25]; fourth, designing dual-layer ceramic coating structures, such as $Gd_2Zr_2O_7$/YSZ [26,27] and $La_2Ce_2O_7$/YSZ [28]; fifth, optimization treatments on the surface of the ceramic coatings, such as reducing the surface

roughness of coatings [29], laser modification [30], and creating micro-nano double-scale structure [31].

In recent years, researches on nanostructure have attracted the interest of a wide range of scholars [32–34]. Li et al. [35] argued that the nano regions in $Gd_2Zr_2O_7$-$LaPO_4$ coatings can impede CMAS infiltration. However, Zhou et al. [36] discovered that nanostructured 8YSZ coatings exhibited a higher amount of m-phase and poorer CMAS corrosion resistance than YSZ coatings after corrosion.

Furthermore, studies on the corrosion resistance of Gd-Yb-Y-stabilized zirconia coatings have diverged. Bahamirian et al. [37] found that APS 9.5Y_2O_3-5.6Yb_2O_3-5.2Gd_2O_3-stabilized ZrO_2 TBCs exhibited superior thermal shock resistance under CMAS exposure compared with YSZ coatings. Li et al. [38] reported that Gd-Yb-YSZ coatings showed better V_2O_5 corrosion resistance than YSZ coatings. On the contrary, Wang et al. [39] reported that the CMAS penetration depth and phase transition were greater in Yb-Gd-YSZ coatings compared with YSZ coatings, indicating lower corrosion resistance.

In this paper, the corrosion behavior and corrosion mechanisms of free-standing YSZ, nanostructured YSZ (n-YSZ), and Gd-Yb-Y stabilized ZrO_2 (GYYSZ) coatings under CMAS exposure at different heat treatment times (5/10/50 h) were investigated in order to verify the CMAS corrosion resistance of all three coatings.

2. Materials and Methods

2.1. Preparation of CMAS Powder

CMAS with a molar ratio of 33CaO-9MgO-13$AlO_{1.5}$-45SiO_2 was used in this study, a composition originally proposed by Borom et al. [40] and subsequently widely used in CMAS-related studies [41]. Figure 1 illustrates the preparation process of the CMAS powder. Firstly, the powders of CaO, MgO, Al_2O_3, and SiO_2 were calcined at 900 °C for a duration of 5 h. Next, the four oxide powders were carefully weighed in accordance with the specified molar ratio and ground using a fast ball mill for 24 h. The mass ratio of powder, grinding medium, and anhydrous ethanol was 1:2:1. The slurry was dried at 120 °C for a period of 6 h, and then the resulting dried powder was sintered at 1150 °C for 24 h in an alumina crucible. Subsequently, the CMAS powder was ball milled and dried for the second time. Finally, the dried CMAS powder was finely ground using a mortar and pestle to obtain the final sample.

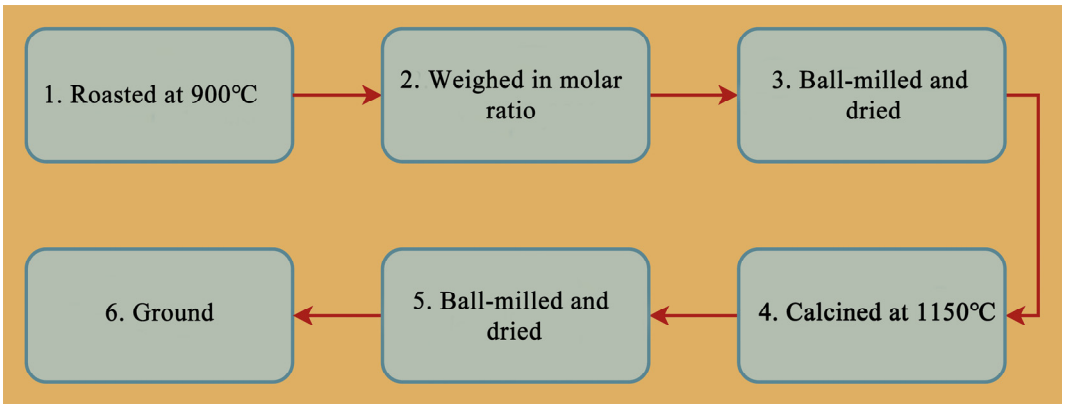

Figure 1. Flowchart of CMAS powder preparation.

2.2. Preparation of Coatings

YSZ, n-YSZ, and GYYSZ coatings were sprayed onto graphite cylinders (φ14.5 mm) by air plasma spraying (APS 2000 A, Beijing, China). Sandpaper was used to sand the edges of the coatings and remove the graphite at the bottom, resulting in free-standing coatings with a diameter of 14 mm. Detailed information of the powders can be found in Table 1, while the spraying parameters can be referenced in Table 2.

Table 1. Powder material for coatings.

Composition (in wt.%)	Granularity (μm)	Manufacturer
6-8Y_2O_3-ZrO_2	20–60	Imerys (Shenyang, China)
Nano 6-8Y_2O_3-ZrO_2	31–63	Shiyuan (Suzhou, China)
5.2Gd_2O_3-5.6Yb_2O_3-9.5Y_2O_3-ZrO_2	30–74	Institute of Metals, China Academy of Sciences (Shenyang, China)

Table 2. Summary of atmospheric plasma spraying parameters.

Parameter	Unit	Value
Voltage	V	70
Current	A	590
Primary gas, Ar	slpm (standard liter per minute)	38
Secondary gas, H_2	slpm (standard liter per minute)	1.8
Spray distance	mm	90

2.3. CMAS Corrosion Experiments

A brush was employed to dip an appropriate amount of powder, with the brush handle gently tapped to evenly disperse the powder, onto the coating surfaces. The coated samples were subsequently weighed multiple times using an electronic balance, ensuring that the deposited amount of CMAS remained within the predetermined range (20 ± 2 mg/cm^2). Given that the melting point of CMAS is generally reported to be approximately 1240 °C [42,43], the coated samples were heat treated at 1250 °C for 5 h, 10 h, and 50 h, respectively.

2.4. Characterization

X-ray diffraction (XRD, SmartLab, Rigaku, Tokyo, Japan) was employed to evaluate the phase composition of the mixed CMAS and YSZ coatings. Microstructural and chemical composition analyses of polished cross-sectional samples of the coatings were performed using an environmental scanning electron microscope (ESEM, XL30-FEG, FEI, Eindhoven, The Netherlands) equipped with an energy dispersive spectrometer (EDS). The average porosity of the coatings was measured using Image J software (Image J 1.8.0, 10 images per sample). The Vickers microhardness of as-sprayed coatings and the coatings after 50 h of corrosion was measured by a Vickers microhardness tester (FALCON 501, INNOVATEST, Maastricht, The Netherlands); according to GB/T 4340.1-2009 standard, six points were tested per sample. A load of 0.3 kg was applied for a duration of 10 s during the loading process.

3. Results

3.1. CMAS Powder

It has been demonstrated that the self-crystallization temperature of CMAS ranges from 950 °C to 1240 °C in previous research [44]. To ensure stability, the CMAS powder was calcined at 1150 °C for 24 h to complete the solid-state reaction. Figure 2 presents the XRD results of the CMAS powder. Upon its subjection to a heat treatment at 1150 °C for a duration of 24 h, three self-crystalline products were formed in the CMAS powder: anorthite ($CaAl_2Si_2O_8$), diopside ($CaMgSi_2O_6$), and wollastonite ($CaSiO_3$). As a result, the obtained CMAS powder demonstrates good stability and fulfills the requirements for CMAS powder composition, making it suitable for subsequent experimental investigations.

3.2. Coatings before and after CMAS Corrosion

3.2.1. Phase Composition

The XRD results of all three as-sprayed coatings are illustrated in Figure 3. Both YSZ and n-YSZ coatings exhibit split peaks at diffraction angles around 35° and 60°, indicating that they are composed of the metastable tetragonal phase (t'-ZrO_2). On the other hand, the GYYSZ

coating exhibits a cubic phase structure (c-ZrO_2). As shown in Figure 4, GYYSZ coatings maintain c-ZrO_2 after exposure to CMAS for 5 h, 10 h, and 50 h. In contrast, the corroded YSZ and n-YSZ coatings exhibit the presence of m-ZrO_2. Notably, the content of m-ZrO_2 is higher in n-YSZ coatings than in YSZ coatings under the same corrosion conditions.

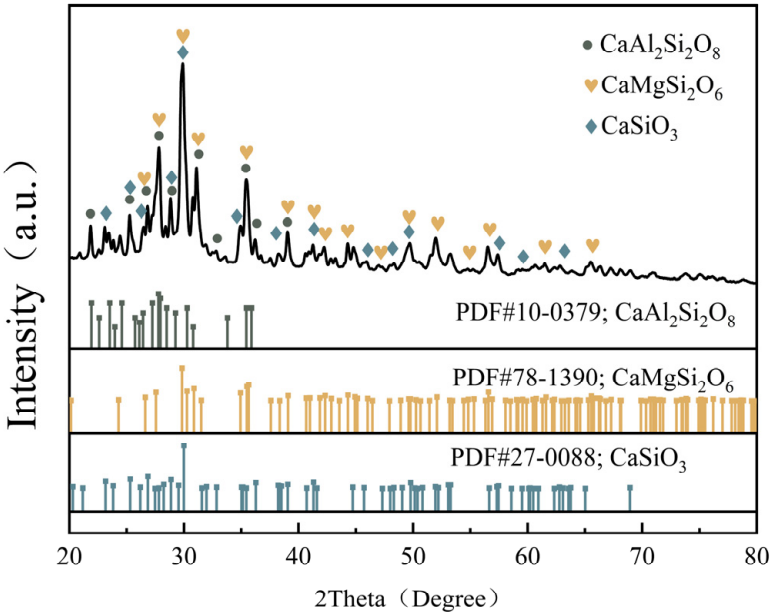

Figure 2. XRD patterns of CMAS powder after calcination at 1150 °C for 24 h.

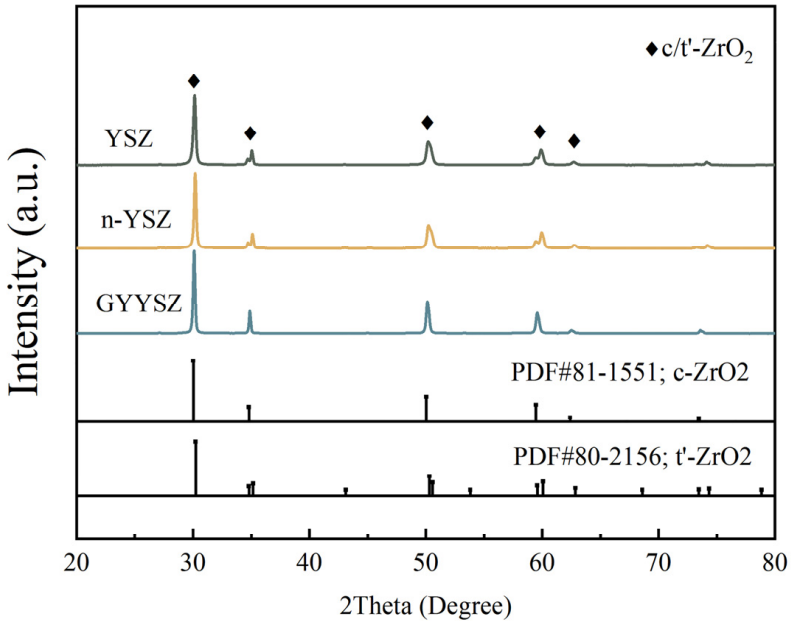

Figure 3. XRD pattern of as-sprayed YSZ, n-YSZ, and GYYSZ coatings.

3.2.2. Microstructure and Chemical Composition

A typical layered structure of APS coatings can be observed in Figure 5, exhibiting numerous horizontal microcracks and pores distributed between the continuous deposition layers. The elemental composition data of the marked regions in Figure 5 are presented in Table 3. The porosities of YSZ, n-YSZ, and GYYSZ coatings were determined to be 7%, 16%, and 13%, respectively. Notably, the gray contrast rough regions in n-YSZ coatings consist of numerous fine, partially melted particles, corresponding to the nanostructured area.

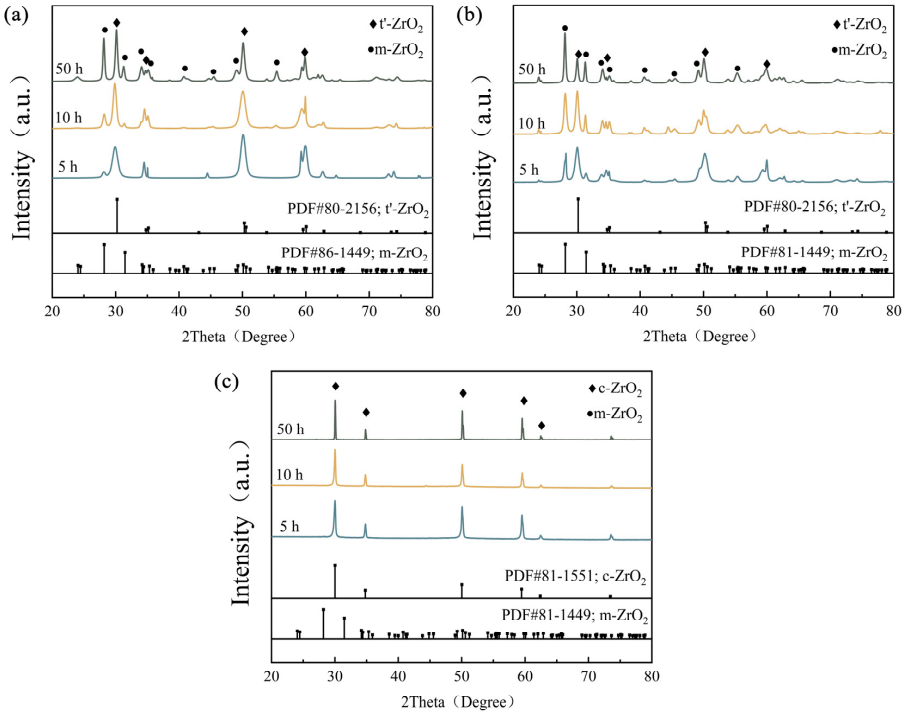

Figure 4. XRD patterns of the coatings after exposure to CMAS at 1250 °C from 5 h to 50 h: (**a**) YSZ coatings, (**b**) n-YSZ coatings, (**c**) GYYSZ coatings.

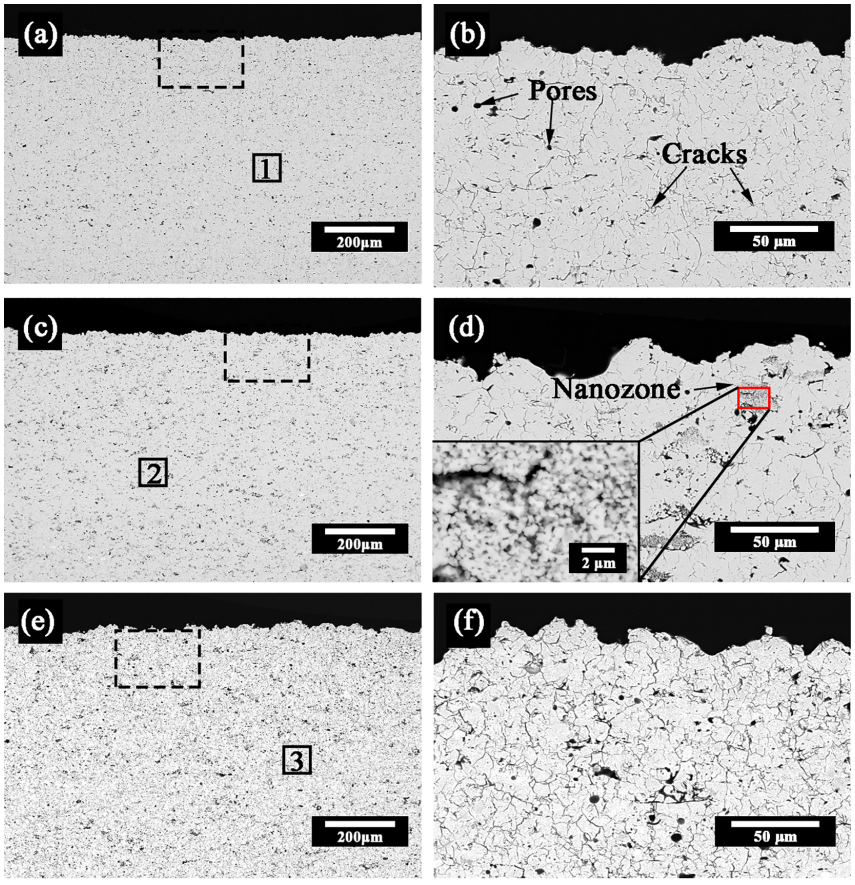

Figure 5. Cross-sectional SEM images of as-sprayed YSZ, n-YSZ, and GYYSZ coatings: (**a**,**b**) YSZ coating, (**c**,**d**) n-YSZ coating, (**e**,**f**) GYYSZ coating.

Table 3. EDS results of marked regions 1–3 in Figure 5.

	Gd (wt.%)	Yb (wt.%)	Y (wt.%)	Zr (wt.%)	O (wt.%)	RE/Zr
1	-	-	6.86	69.43	23.71	0.10
2	-	-	7.12	69.31	23.58	0.10
3	5.54	6.06	8.98	58.93	20.50	0.35

Figures 6 and 7 illustrate the cross-sectional morphologies of YSZ and n-YSZ coatings after exposure to CMAS for 5 h, 10 h, and 50 h. The elemental composition data of the marked regions are presented in Table 4. A dark gray layer (Region 1 in Figure 6) is formed on the corroded coating surface, primarily consisting of Ca and Si elements, indicating the presence of residual CMAS. The thickness of the CMAS layer decreases with corrosion time. The surface lamellar structure of the coating is disrupted, resulting in the formation of numerous fine spherical particles that constitute a loosely arranged layer referred to as the "loose layer." The thickness of the loose layer increases with corrosion time. Based on the EDS and XRD results, the spherical particles (Region 3 in Figure 6; Region 5 in Figure 7) can be inferred as ZrO_2. Comparing the spheroidized regions within the coatings (Region 3 in Figure 6 and Region 5 in Figure 7) to the un-spheroidized regions (Region 2 in Figure 6 and Region 4 in Figure 7), lower RE/Zr ratios and higher CMAS content are found in the spheroidized regions, indicating more severe corrosion in the loose layer. Notably, the n-YSZ coatings exhibit earlier peeling and disappearance of the residual CMAS layer compared with the YSZ coatings.

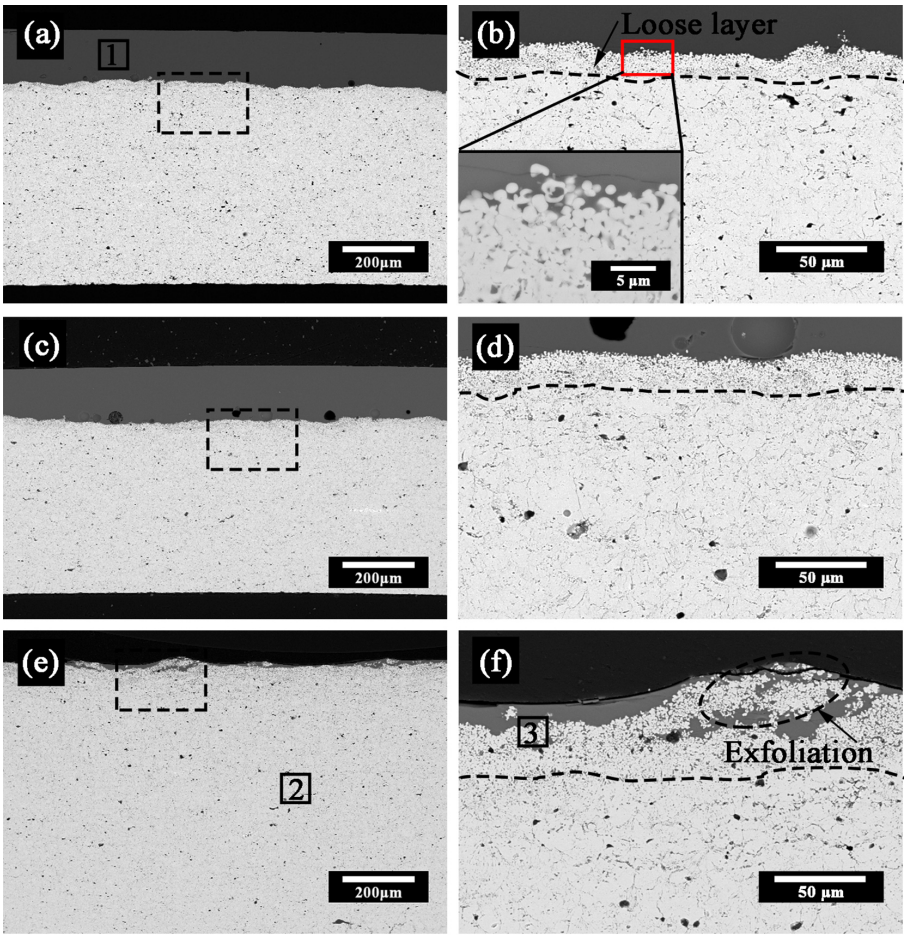

Figure 6. Cross-sectional SEM images of YSZ coatings after exposure to CMAS at 1250 °C from 5 h to 50 h: (**a**,**b**) 5 h, (**c**,**d**) 10 h, (**e**,**f**) 50 h.

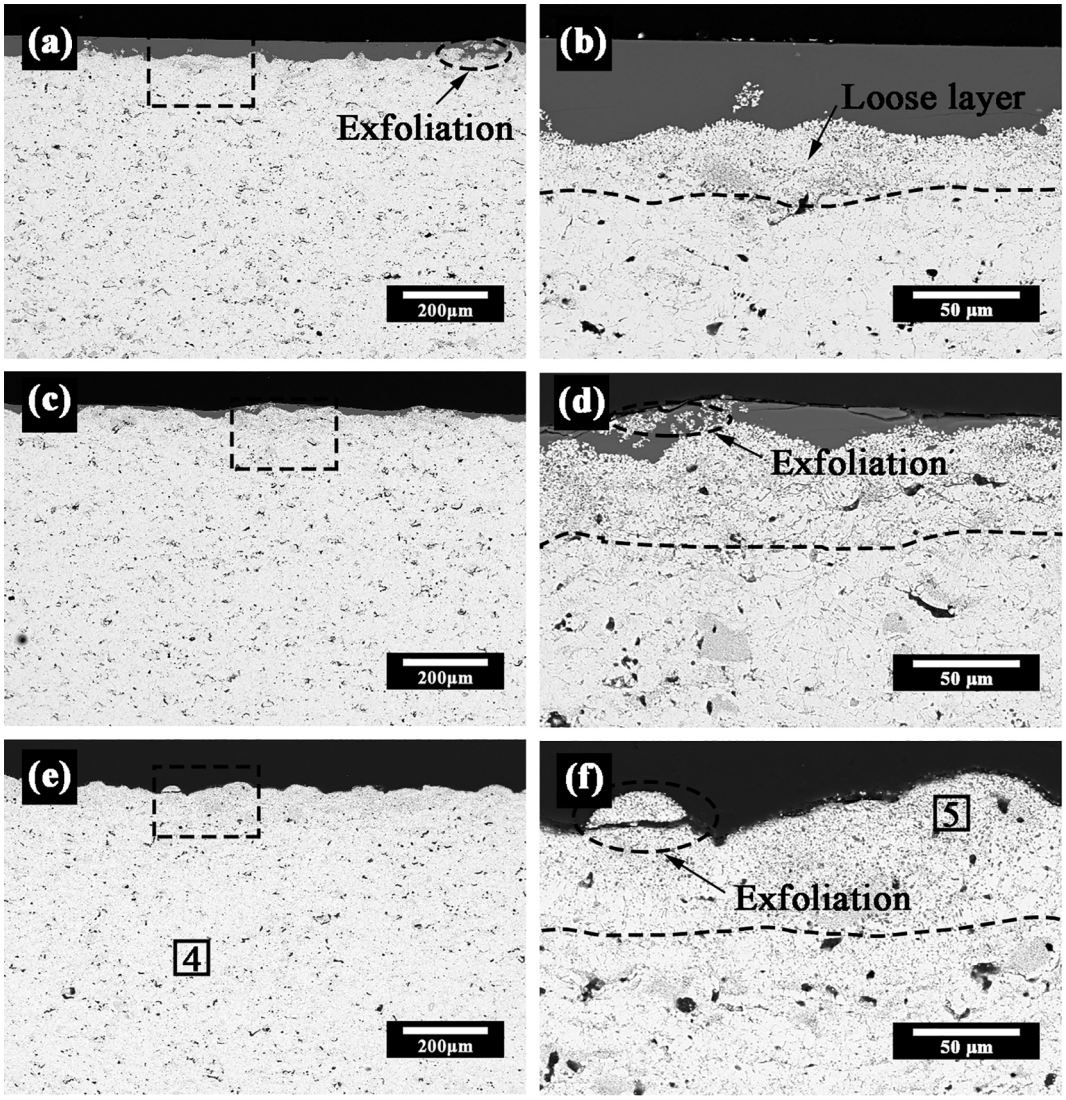

Figure 7. Cross-sectional SEM images of n-YSZ coatings after exposure to CMAS at 1250 °C from 5 h to 50 h: (**a**,**b**) 5 h, (**c**,**d**) 10 h, (**e**,**f**) 50 h.

Table 4. EDS results of marked regions 1–7 in Figures 6–8.

	Gd (wt.%)	Yb (wt.%)	Y (wt.%)	Zr (wt.%)	Ca (wt.%)	Mg (wt.%)	Al (wt.%)	Si (wt.%)	O (wt.%)	RE/Zr
1	-	-	1.33	3.48	23.11	3.72	7.34	20.20	40.82	0.38
2	-	-	5.75	67.11	1.39	0.29	0.56	1.70	23.21	0.09
3	-	-	3.09	66.82	2.33	0.37	0.79	2.61	23.99	0.05
4	-	-	4.86	66.68	1.65	0.37	0.63	2.03	23.78	0.07
5	-	-	2.90	61.69	3.05	0.57	1.08	3.27	27.44	0.05
6	4.79	5.38	8.53	58.16	0.79	0.18	0.20	0.85	21.13	0.32
7	4.76	5.19	8.23	58.65	1.31	0.18	0.27	1.14	20.27	0.31

Figure 8 illustrates the cross-sectional morphologies of GYYSZ coatings after exposure to CMAS for 5 h, 10 h, and 50 h. The elemental composition data of the marked regions are presented in Table 4. Spherical particles were also observed on the surface of the GYYSZ coating, with some of these particles diffusing into the CMAS layer. The RE/Zr ratios of GYYSZ coatings on the surface (Region 7) and inside (Region 6) are very similar, indicating that the surface of GYYSZ coating is not loose. The residual CMAS layer with pores and coarse spherical particles is still on the surface of GYYSZ coatings after 50 h of corrosion.

Please note that the dark contrast material inside the pores in the figure is epoxy resin, which may have infiltrated the pores during the sample embedding process.

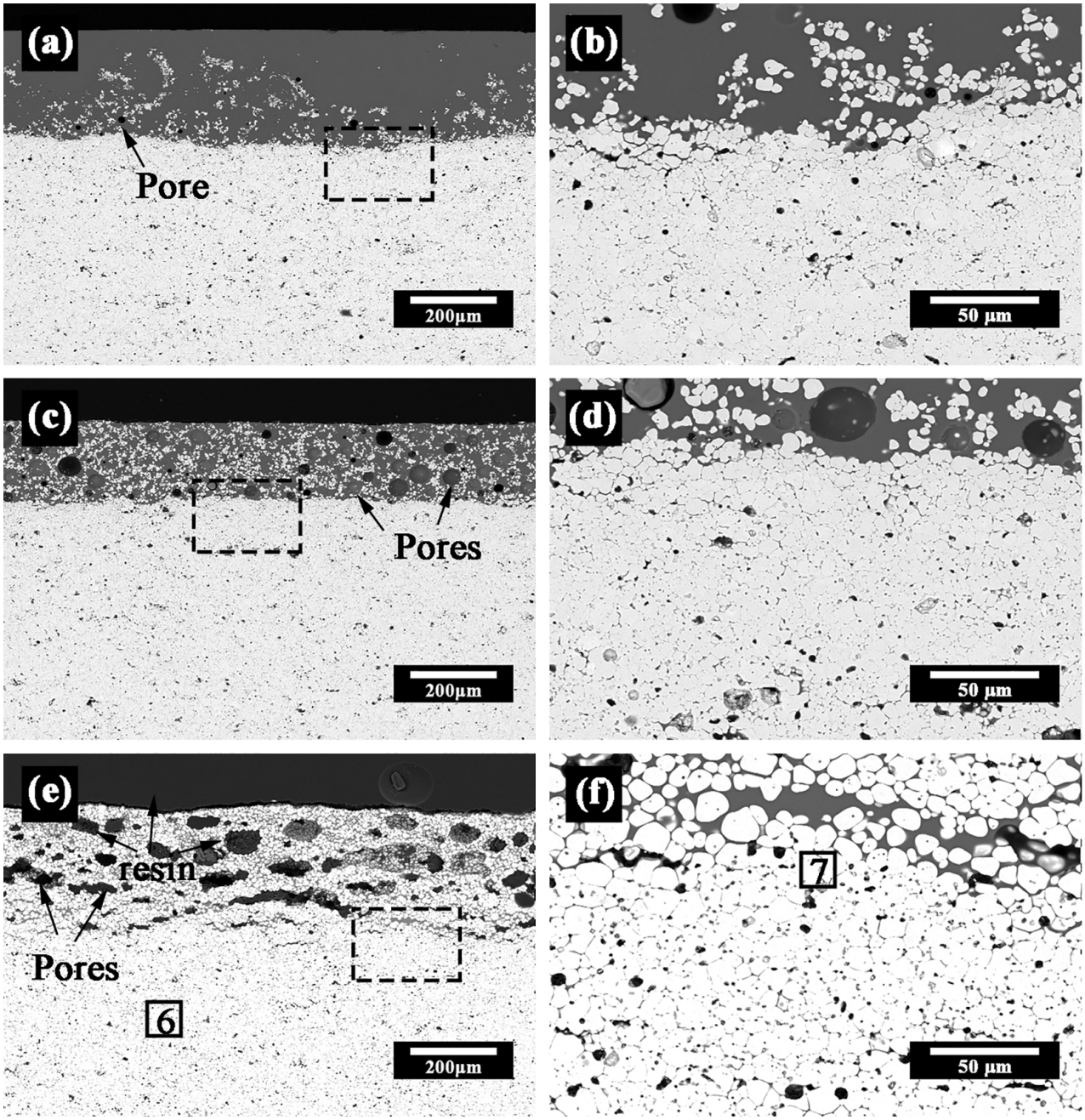

Figure 8. Cross-sectional SEM images of GYYSZ coatings after exposure to CMAS at 1250 °C from 5 h to 50 h: (**a**,**b**) 5 h, (**c**,**d**) 10 h, (**e**,**f**) 50 h.

The enlarged cross-sectional morphologies of all three coatings after 5 h, 10 h, and 50 h of corrosion are shown in Figure 9. The elemental composition data of the marked regions are presented in Table 5. The size and quantity of spherical particles in all three coatings increase with corrosion time (Points 2–4 in YSZ coatings, Points 5–7 in n-YSZ coatings, Points 8–10 in GYYSZ coatings). The content of rare earth elements is lower in the fine spherical particles of YSZ and n-YSZ coatings (Points 2–7), while the content in the coarse spherical particles of GYYSZ coatings (Points 8–10) is higher. Additionally, the RE/Zr ratio within the CMAS layer (Point 1) is higher compared with the as-sprayed coatings,

indicating a significant diffusion of rare earth elements into the CMAS layer, leading to a decrease in the rare earth content of the spherical particles.

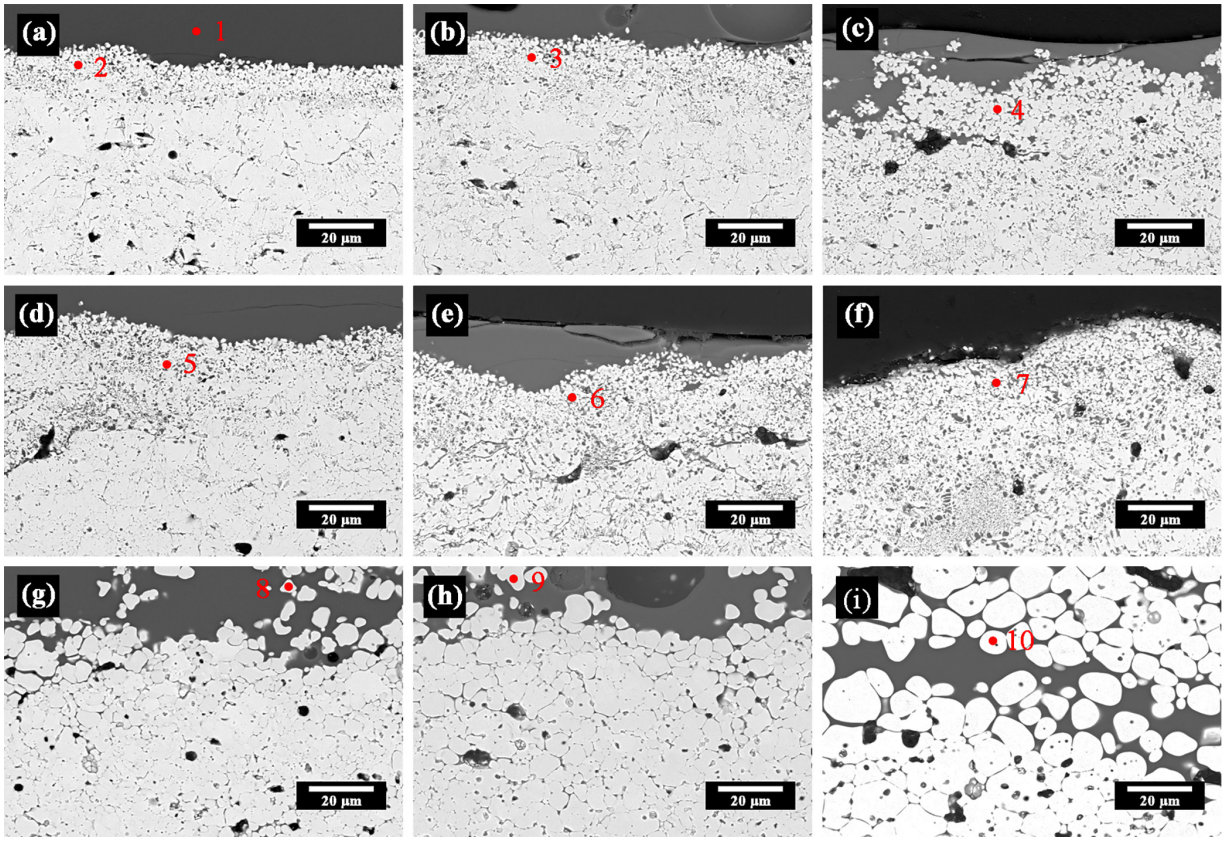

Figure 9. Cross-sectional SEM images of YSZ, n-YSZ, and GYYSZ coatings with higher magnification after exposure to CMAS at 1250 °C for 5 h, 10 h, and 50 h: (**a**–**c**) YSZ coatings, (**d**–**f**) n-YSZ coatings, (**g**–**i**) GYYSZ coatings.

Table 5. EDS results of marked regions 1–10 in Figure 9.

	Gd (wt.%)	Yb (wt.%)	Y (wt.%)	Zr (wt.%)	Ca (wt.%)	Mg (wt.%)	Al (wt.%)	Si (wt.%)	O (wt.%)	RE/Zr
1	-	-	1.36	3.17	23.20	3.79	7.31	20.11	41.06	0.43
2	-	-	3.19	66.79	1.80	0.36	0.62	1.88	25.35	0.05
3	-	-	3.02	72.07	0.73	0.21	0.30	1.00	22.67	0.04
4	-	-	2.45	65.71	2.13	0.53	0.80	2.29	26.09	0.04
5	-	-	2.63	55.62	5.96	0.96	2.02	5.77	27.04	0.05
6	-	-	2.61	67.67	1.50	0.23	0.48	1.72	25.80	0.04
7	-	-	2.83	78.85	0.59	0	0.01	0.79	16.93	0.04
8	5.30	5.66	8.49	58.57	0.63	0.20	0.10	0.55	20.50	0.33
9	4.39	5.14	8.16	61.27	1.12	0.10	0.04	0.51	19.28	0.29
10	3.43	4.55	6.75	55.46	3.09	0.44	0.62	2.11	23.55	0.27

3.2.3. Microhardness

The microhardness of YSZ, n-YSZ, and GYYSZ coatings before and after corrosion are shown in Figure 10. The initial microhardness of the as-sprayed coatings ranges from 600 to 850 HV0.3. After 50 h of CMAS corrosion, the microhardness increases to a range of 1000–1200 HV0.3. This rise in microhardness can be attributed to the combined effects of CMAS corrosion and high-temperature sintering. Specifically, the microhardness increases by 44% in YSZ coatings, 79% in n-YSZ coatings, and relatively minorly by 35% in GYYSZ coatings.

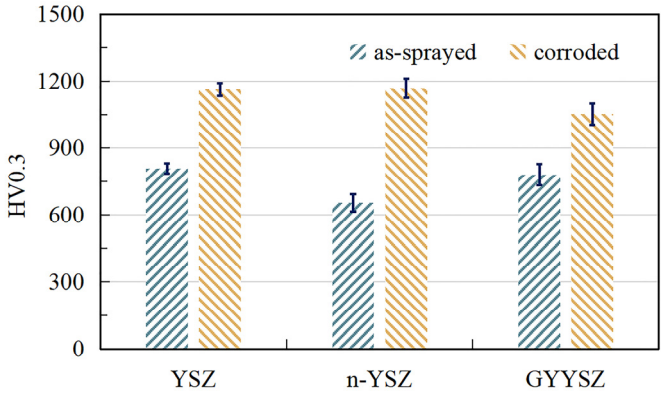

Figure 10. The microhardness for as-sprayed and 50 h corrosion samples of YSZ, n-YSZ, and GYYSZ coatings.

4. Discussion

4.1. Penetration Depth

The following formula can be used to estimate the depth, (L), of penetration of a well-wetted fluid into a porous medium by capillary action [43,45]:

$$t = \left[\frac{k_t}{8D_c}\left(\frac{1-\omega}{\omega}\right)L^2\right]\frac{\eta}{\sigma_{LV}} \quad (1)$$

In this equation, k_t represents the curvature factor (4), indicating the curvature of the capillary. Larger values of k_t indicate higher curvature. D_c is the capillary diameter (1 µm); ω represents the porosity of the loose medium (7%–16%); η represents the fluid viscosity (14 N s/m^2) [43,46]; and σ_{LV} represents the fluid surface tension (0.4 J/m^2) [43].

Based on the Formula (1), the estimated times for CMAS melt to penetrate a depth of 1 mm into YSZ, n-YSZ, and DYSZ coatings were 91.88 s, 232.5 s, and 117.12 s, respectively. This indicates a rapid and extensive penetration of the entire ceramic layer by CMAS when it is molten at 1250 °C. As shown in Figure 11, the EDS results at different depths of the YSZ coating after 5 h of corrosion reveal no significant difference on the content of CMAS along the depth. This suggests that CMAS has fully penetrated throughout the coatings, rendering the penetration depth an ineffective measure of corrosion resistance in this study. The CMAS corrosion behavior of the coatings will be analyzed next by comparing the degree of phase transition and microstructure of the coatings.

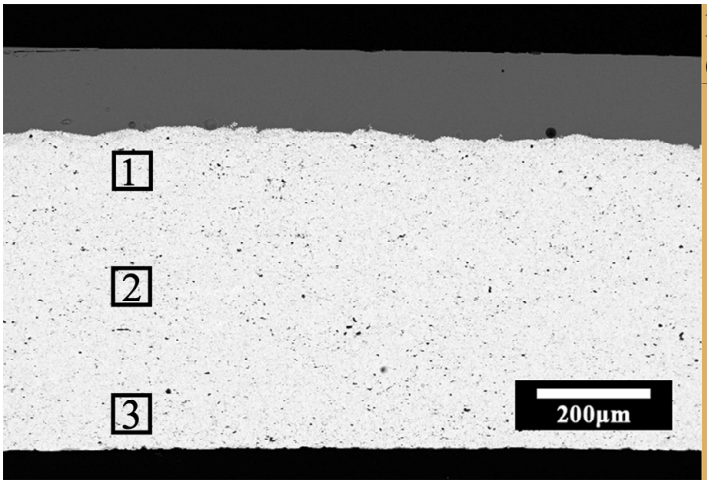

Element (wt.%)	1	2	3
Y	6.14	7.16	7.23
Zr	64.88	66.91	66.81
Ca	1.68	0.69	0.70
Mg	0.37	0.23	0.22
Al	0.67	0.30	0.40
Si	1.82	1.04	1.04
O	24.44	23.67	23.60

Figure 11. Cross-sectional SEM images and EDS results of YSZ coatings exposed to CMAS at 1250 °C for 5 h.

4.2. Coatings Densification

Compared with the as-sprayed coatings, a significant decrease in porosity is observed in the corroded coatings, which is consistent with findings reported in other literature [47,48]. The porosities of YSZ, n-YSZ, and GYYSZ coatings decrease from their initial values of 0.07, 0.16, and 0.13 to 0.05, 0.09, and 0.10 after 50 h of corrosion, respectively.

The densification of the coatings can be attributed to three primary mechanisms. Firstly, sintering occurs within the coatings at elevated temperature, leading to an increased density. Secondly, molten CMAS infiltrates the coatings through pores and cracks, filling these voids and consequently enhancing densification. Thirdly, a phase transition occurs within the coatings following CMAS corrosion, leading to volume expansion and further densification. This phase transition brings about negative effects in the coatings, including reduced stress tolerance and heightened thermal conductivity and hardness. As a result, it is tentatively inferred that GYYSZ coatings demonstrate superior resistance to CMAS corrosion compared with YSZ coatings, while n-YSZ coatings exhibit relatively weaker resistance.

4.3. Phase Transition and Spheroidization

A transition from the t'-ZrO_2 to the m-ZrO_2 can be found during cooling, probably due to the reduction of stabilizers in YSZ and n-YSZ coatings under CMAS exposure (Figure 4a,b). Unfortunately, this phase transition adversely affects the service life of the coatings [49]. In contrast, there is no phase transition in GYYSZ coatings under the same conditions (Figure 4c). To assess the CMAS corrosion behavior of YSZ and n-YSZ coatings, the m phase content in the corroded samples was calculated by Equation (2) [50]:

$$m\% = \frac{I_{m(-111)} + I_{m(111)}}{I_{m(-111)} + I_{m(111)} + I_{t(101)}} \times 100\% \quad (2)$$

The m phase content in YSZ and n-YSZ coatings increases with corrosion time, as shown in Figure 12a. Notably, the m phase content in n-YSZ coatings is higher compared with YSZ coatings under the same corrosion conditions. This observation implies that GYYSZ coatings exhibit superior corrosion resistance in comparison with YSZ coatings, while, conversely, the corrosion resistance of n-YSZ coatings appears to be comparatively weaker.

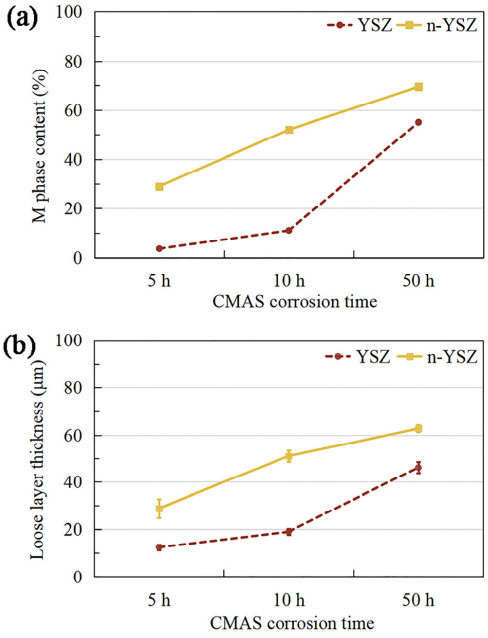

Figure 12. M-phase content (**a**) and loose layer thickness (**b**) as a function of corrosion time at 1250 °C for the coatings of YSZ and n-YSZ.

Spheroidization can be observed in corroded coatings. Specifically, large fine spherical particles with a low content of rare earth elements are formed in YSZ and n-YSZ coatings, collectively contributing to the formation of the loose layer. In contrast, numerous coarse spherical particles with a high content of rare earth elements are observed in GYYSZ coatings. This spheroidization phenomena can potentially be attributed to the continuous dissolution of the coatings under CMAS exposure, leading to the destruction of their lamellar structure and subsequent gradual evolution into spherical particles. Additionally, spherical particles are also formed during dissolution–reprecipitation in the coatings [43]. As shown in Figure 12, the thickness of the loose layer in YSZ and n-YSZ coatings increases with corrosion time, similar to the trend observed in the phase transition. This observation suggests that the fine spherical particles within the loose layer may correspond to the m-ZrO_2.

4.4. Corrosion Mechanisms

According to the study conducted by Stott et al. [51], it is demonstrated that the diffusion rate within glass increases with the content of modifiers, such as Y_2O_3 and other rare earth oxides. Consequently, the coatings with different compositions exhibit varying diffusion rates after dissolution in CMAS, as shown in Figure 13.

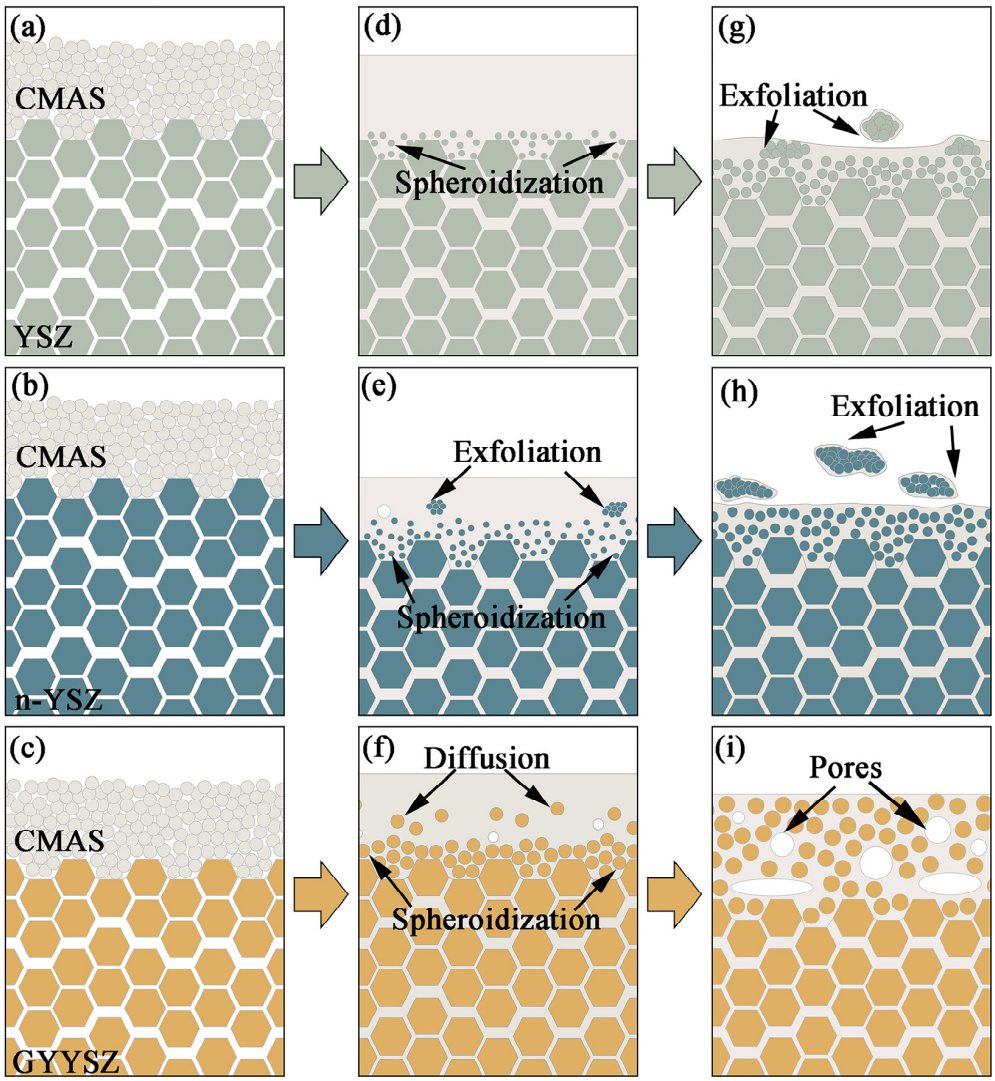

Figure 13. CMAS corrosion mechanisms of YSZ, n-YSZ, and GYYSZ coatings: (**a**–**c**) before CMAS attack, (**d**–**f**) after short-term CMAS attack, (**g**–**i**) after long-term CMAS attack.

For YSZ coatings, the CMAS corrosion mechanism primarily involves the thermo-mechanical and thermo-chemical processes. In terms of the thermo-mechanical aspect [52], CMAS infiltrates the ceramic layer through capillary action and solidifies upon cooling, filling the pores and cracks within the coatings. This leads to a reduction in the properties of the coating and contributes to cracking. In terms of the thermo-chemical aspect [53,54], CMAS corrodes the coatings through a dissolution–precipitation mechanism. As the coatings dissolve in CMAS, ZrO_2 becomes saturated in CMAS first due to the higher diffusion coefficient of Y^{3+} compared with Zr^{4+} and the greater solubility of Y_2O_3 in molten CMAS in comparison with ZrO_2 [51]. Subsequently, the coatings resolved in CMAS re-precipitate as Y-lean ZrO_2, resulting in a transition from t'-ZrO_2 to m-ZrO_2 during cooling. This phase transition induces a volume change of approximately 3%–5% within the coatings, generating significant stress. When the stress surpasses the critical threshold, the coatings undergo exfoliation, ultimately leading to failure.

In this study, the failure primarily occurs at the surface of the coatings, with no significant changes in the interior. This can be attributed to direct contact between the coating surfaces and large CMAS chunks. The Y_2O_3 in the substantial CMAS chunks struggles to reach saturation, resulting in the continuous dissolution of YSZ particles and accelerated diffusion of Y^{3+} into CMAS. This process leads to reduced phase stability of YSZ particles of the coating surfaces. In contrast, Y_2O_3 saturation in the infiltrated CMAS in the interior of the coatings is achieved more readily. This is attributed to the lower CMAS content in the interior of the coatings and the higher quantity of YSZ particles. Consequently, the Y content of YSZ particles in the interior of the coatings undergoes minimal changes and remains relatively stable, rendering them less prone to phase transition [55].

For n-YSZ coatings, the corrosion mechanism is similar to that of YSZ coatings. However, the performances are poorer in n-YSZ coatings compared with YSZ coatings under identical CMAS conditions. For example, n-YSZ coatings exhibit thicker loose layers, earlier disappearance of residual CMAS on the surface, and an earlier onset of exfoliation. This disparity can be attributed to the smaller grain size and larger specific surface area of n-YSZ in comparison with YSZ. The increased contact area between n-YSZ and CMAS results in a higher interaction, rendering n-YSZ more susceptible to CMAS attack [36].

The corrosion mechanism of GYYSZ coatings differs from that of YSZ and n-YSZ coatings, primarily due to the high content of rare earth elements. This prevents ZrO_2 from saturating before Y_2O_3 in CMAS, thereby impeding the re-precipitation as Y-lean ZrO_2 and maintaining coarse spherical particles with a high content of rare earth elements. Additionally, the high concentration of modifiers in GYYSZ coatings also accelerates the diffusion rate of coating elements into CMAS. Consequently, the diffusion of the coatings into CMAS is more pronounced in GYYSZ coatings compared with YSZ and n-YSZ coatings [51].

The study demonstrated that the CMAS resistance of GYYSZ coatings outperforms that of YSZ coatings, while that of n-YSZ coatings is inferior. These results provide valuable insights into the behavior and mechanisms of CMAS corrosion in n-YSZ and GYYSZ coatings and contribute to the development of novel materials in the field of TBCs.

5. Conclusions

In this paper, a comprehensive study was conducted to investigate the CMAS corrosion behavior and corrosion mechanisms of n-YSZ and GYYSZ coatings. By comparing them with YSZ coatings, several important conclusions can be drawn:

1. Decreased porosity and increased microhardness are found in all three coatings after CMAS corrosion. The increase in microhardness of n-YSZ coatings is more pronounced than that of YSZ coatings, while that of GYYSZ coatings is relatively small.
2. Loose layers consisting of fine spherical m-ZrO_2 particles are formed in both corroded n-YSZ and YSZ coatings. The thickness of loose layers and the degree of phase transition in the coatings increase with corrosion time. More pronounced phase transition and earlier spalling are observed in n-YSZ coatings compared with YSZ coatings.

3. No phase transition or exfoliation occurs in GYYSZ coating. Instead, the formation of coarse spherical particles in the coatings and diffusion into CMAS are observed.
4. The CMAS corrosion resistance of the coatings follows the order: GYYSZ > YSZ > n-YSZ. Doping ZrO_2 with Gd/Yb/Y elements enhances both the phase stability and the resistance to CMAS corrosion of the coatings.

Author Contributions: Conceptualization and supervision, N.X.; investigation and writing—original draft preparation, L.Z.; writing—review and editing, M.G.; literature search and funding acquisition, J.Z.; resources, X.C. All authors have read and agreed to the published version of the manuscript.

Funding: This work was supported by the Key Research Program of the Chinese Academy of Sciences (Grant NO. ZDRW-CN-2021-2-2) and IMR Innovation Fund (2022-PY08).

Institutional Review Board Statement: Not applicable.

Informed Consent Statement: Not applicable.

Data Availability Statement: Not applicable.

Conflicts of Interest: The authors declare no conflict of interest.

References

1. Padture, N.P.; Gell, M.; Jordan, E.H. Thermal Barrier Coatings for Gas-Turbine Engine Applications. *Science* **2002**, *296*, 280–284. [CrossRef]
2. Wei, Z.-Y.; Meng, G.-H.; Chen, L.; Li, G.-R.; Liu, M.-J.; Zhang, W.-X.; Zhao, L.-N.; Zhang, Q.; Zhang, X.-D.; Wan, C.-L.; et al. Progress in Ceramic Materials and Structure Design toward Advanced Thermal Barrier Coatings. *J. Adv. Ceram.* **2022**, *11*, 985–1068. [CrossRef]
3. Li, P.; Jin, X.; Lu, P.; Liu, D.; Mou, R.; Fan, X. Comparative Study on Microstructure Evolution and Failure Mechanisms of Ordinary and Refurbished EB-PVD TBC under Cyclic Oxidation. *J. Adv. Ceram.* **2023**. [CrossRef]
4. Chinnusamy, S.; Ramasamy, V.; Venkatajalapathy, S.; Kaliyannan, G.V.; Palaniappan, S.K. Experimental Investigation on the Effect of Ceramic Coating on the Wear Resistance of Al6061 Substrate. *J. Mater. Res. Technol.* **2019**, *8*, 6125–6133. [CrossRef]
5. Bakan, E.; Vaßen, R. Ceramic Top Coats of Plasma-Sprayed Thermal Barrier Coatings: Materials, Processes, and Properties. *J. Therm. Spray Tech.* **2017**, *26*, 992–1010. [CrossRef]
6. Naumenko, D.; Pillai, R.; Chyrkin, A.; Quadakkers, W.J. Overview on Recent Developments of Bondcoats for Plasma-Sprayed Thermal Barrier Coatings. *J. Therm. Spray Tech.* **2017**, *26*, 1743–1757. [CrossRef]
7. Saillard, A.; Cherkaoui, M.; Capolungo, L.; Busso, E.P. Stress Influence on High Temperature Oxide Scale Growth: Modeling and Investigation on a Thermal Barrier Coating System. *Philos. Mag.* **2010**, *90*, 2651–2676. [CrossRef]
8. Li, C.L.; Wang, W.; Tan, S.L.; Song, S.G. Bond Strength and Oxidation Resistance of YSZ/(Ni, Al) Composite Coatings. *Surf. Eng.* **2014**, *30*, 619–623. [CrossRef]
9. Witz, G.; Shklover, V.; Steurer, W.; Bachegowda, S.; Bossmann, H.-P. Phase Evolution in Yttria-Stabilized Zirconia Thermal Barrier Coatings Studied by Rietveld Refinement of X-Ray Powder Diffraction Patterns. *J. Am. Ceram. Soc.* **2007**, *90*, 2935–2940. [CrossRef]
10. Cheng, B.; Zhang, Y.-M.; Yang, N.; Zhang, M.; Chen, L.; Yang, G.-J.; Li, C.-X.; Li, C.-J. Sintering-Induced Delamination of Thermal Barrier Coatings by Gradient Thermal Cyclic Test. *J. Am. Ceram. Soc.* **2017**, *100*, 1820–1830. [CrossRef]
11. Hayashi, Y.; Lokachari, S.; Yamagishi, S.; Okazaki, M. CMAS Damage in Thermal Barrier Coatings: An Exploration via Single Crystal Bulk YSZ Specimen. *Mech. Eng. Lett.* **2016**, *2*, 16–00240. [CrossRef]
12. Wu, Y.; Luo, H.; Cai, C.; Wang, Y.; Zhou, Y.; Yang, L.; Zhou, G. Comparison of CMAS Corrosion and Sintering Induced Microstructural Characteristics of APS Thermal Barrier Coatings. *J. Mater. Sci. Technol.* **2019**, *35*, 440–447. [CrossRef]
13. Satpathy, R.; Rani, S.; Alam, Z.; Besra, L. Effectiveness of Lanthanum Zirconate and Yttria Stabilised Zirconia Freestanding APS Thermal Barrier Coatings against Natural CMAS Attack at High Temperatures. *Mater. High. Temp.* **2020**, *37*, 416–424. [CrossRef]
14. Wang, H.; Sheng, Z.; Tarwater, E.; Zhang, X.; Fergus, J.W. Function of Reaction Layer in Pyrochlore Thermal Barrier Coatings against CMAS Corrosion. *ECS Trans.* **2015**, *66*, 53–59. [CrossRef]
15. Deng, W.; Fergus, J.W. Effect of CMAS Composition on Hot Corrosion Behavior of Gadolinium Zirconate Thermal Barrier Coating Materials. *J. Electrochem. Soc.* **2017**, *164*, C526–C531. [CrossRef]
16. Wang, F.; Guo, L.; Wang, C.; Ye, F. Calcium-Magnesium-Alumina-Silicate (CMAS) Resistance Characteristics of $LnPO_4$ (Ln = Nd, Sm, Gd) Thermal Barrier Oxides. *J. Eur. Ceram. Soc.* **2017**, *37*, 289–296. [CrossRef]
17. Guo, L.; Yan, Z.; Wang, X.; He, Q. Ti_2AlC MAX Phase for Resistance against CMAS Attack to Thermal Barrier Coatings. *Ceram. Int.* **2019**, *45*, 7627–7634. [CrossRef]
18. Liu, S.; Liu, Q.; Hu, X.; Guo, J.; Zhu, W.; Zhang, F.; Xia, J. CMAS Corrosion Resistance Behavior and Mechanism of $Hf_6Ta_2O_{17}$ Ceramic as Potential Material for Thermal Barrier Coatings. *Coatings* **2023**, *13*, 404. [CrossRef]
19. Boissonnet, G.; Chalk, C.; Nicholls, J.R.; Bonnet, G.; Pedraza, F. Thermal Insulation of YSZ and Erbia-Doped Yttria-Stabilised Zirconia EB-PVD Thermal Barrier Coating Systems after CMAS Attack. *Materials* **2020**, *13*, 4382. [CrossRef]

20. Fan, W.; Bai, Y.; Liu, Y.F.; Kang, Y.X.; Wang, Y.; Wang, Z.Z.; Tao, W.Z. Corrosion Behavior of Sc_2O_3–Y_2O_3 Co-Stabilized ZrO_2 Thermal Barrier Coatings with CMAS Attack. *Ceram. Int.* **2019**, *45*, 15763–15767. [CrossRef]
21. Bal, E.; Karabaş, M.; Yılmaz Taptık, İ. The Effect of CMAS Interaction on Thermal Cycle Lifetime of YSZ Based Thermal Barrier Coatings. *Mater. Res. Express* **2018**, *5*, 065201. [CrossRef]
22. Wang, Z.; Zhang, J.; Han, S.; Liu, J. Corrosion Resistance of Modified YSZ Coatings Subjected to CMAS Attacks. *Surf. Eng.* **2022**, *38*, 393–401. [CrossRef]
23. Yuan, K.; Yang, L.; Wang, Q.; Zhang, F.; Zhu, W.; Zhou, Y. Al_2O_3–TiO_2 Codoped Yttria-Stabilized Zirconia Thermal Barrier Coatings Resistant to Damage by Molten Calcium-Magnesium-Alumino-Silicate (CMAS) Glass. *Adv. Eng. Mater.* **2021**, *23*, 2001338. [CrossRef]
24. Liu, H.; Cai, J.; Zhu, J. CMAS (CaO–MgO–Al_2O_3–SiO_2) Resistance of Y_2O_3-Stabilized ZrO_2 Thermal Barrier Coatings with Pt Layers. *Ceram. Int.* **2018**, *44*, 452–458. [CrossRef]
25. Zhang, X.; Zhou, K.; Xu, W.; Chen, B.; Song, J.; Liu, M. In Situ Synthesis of α-Alumina Layer on Thermal Barrier Coating for Protection against CMAS (CaO–MgO–Al_2O_3–SiO_2) Corrosion. *Surf. Coat. Technol.* **2015**, *261*, 54–59. [CrossRef]
26. Jonnalagadda, K.P.; Peng, R.L.; Mahade, S.; Markocsan, N.; Nylén, P.; Björklund, S.; Curry, N.; Li, X.-H. Hot Corrosion Behavior of Multi-Layer Suspension Plasma Sprayed $Gd_2Zr_2O_7$/YSZ Thermal Barrier Coatings. *Interceram-Int. Ceram. Rev.* **2017**, *66*, 180–184. [CrossRef]
27. Mahade, S.; Curry, N.; Björklund, S.; Markocsan, N.; Joshi, S. Durability of Gadolinium Zirconate/YSZ Double-Layered Thermal Barrier Coatings under Different Thermal Cyclic Test Conditions. *Materials* **2019**, *12*, 2238. [CrossRef] [PubMed]
28. Kang, Y.X.; Bai, Y.; Wang, Y.; Su, X.L. Degradation and Failure of a Novel Double-Layer LC/YSZ Thermal Barrier Coating in a Burner Rig Corrosion Test. *Mater. High Temp.* **2023**, 1–14. [CrossRef]
29. Guo, L.; Li, G.; Gan, Z. Effects of Surface Roughness on CMAS Corrosion Behavior for Thermal Barrier Coating Applications. *J. Adv. Ceram.* **2021**, *10*, 472–481. [CrossRef]
30. Avcı, A.; Karabaş, M.; Akdoğan Eker, A.; Akman, E.; Aslan, C. Hot Corrosion and CMAS Degradation of Laser-Glazed YSZ Coating with Optimum Parameter. *Proc. Inst. Mech. Eng. Part L J. Mater. Des. Appl.* **2023**, 146442072311781. [CrossRef]
31. Wang, Y.; Xu, Z.; Wang, W.; Zhang, C.; Yu, Z.; Fang, H.; Yang, T. Preparation and CMAS Wettability Investigation of CMAS Corrosion Resistant Protective Layer with Micro-Nano Double Scale Structure. *Coatings* **2022**, *12*, 648. [CrossRef]
32. Moriarty, P. Nanostructured Materials. *Rep. Prog. Phys.* **2001**, *64*, 297–381. [CrossRef]
33. Malkiel, I.; Mrejen, M.; Nagler, A.; Arieli, U.; Wolf, L.; Suchowski, H. Plasmonic Nanostructure Design and Characterization via Deep Learning. *Light Sci. Appl.* **2018**, *7*, 60. [CrossRef] [PubMed]
34. Velu Kaliyannan, G.; Palanisamy, S.V.; Rathanasamy, R.; Palanisamy, M.; Palaniappan, S.K.; Chinnasamy, M. Influence of Ultrathin Gahnite Anti-Reflection Coating on the Power Conversion Efficiency of Polycrystalline Silicon Solar Cell. *J. Mater. Sci. Mater. Electron.* **2020**, *31*, 2308–2319. [CrossRef]
35. Li, M.; Cheng, Y.; Guo, L.; Zhang, Y.; Zhang, C.; He, S.; Sun, W.; Ye, F. Preparation of Nanostructured $Gd_2Zr_2O_7$-$LaPO_4$ Thermal Barrier Coatings and Their Calcium-Magnesium-Alumina-Silicate (CMAS) Resistance. *J. Eur. Ceram. Soc.* **2017**, *37*, 3425–3434. [CrossRef]
36. Zhou, X.; Chen, T.; Yuan, J.; Deng, Z.; Zhang, H.; Jiang, J.; Cao, X. Failure of Plasma Sprayed Nano-zirconia-based Thermal Barrier Coatings Exposed to Molten CaO-MgO-Al_2O_3-SiO_2 Deposits. *J. Am. Ceram. Soc.* **2019**, *102*, 6357–6371. [CrossRef]
37. Bahamirian, M.; Hadavi, S.M.M.; Farvizi, M.; Keyvani, A.; Rahimipour, M.R. Hot Corrosion Behavior of ZrO_2 $9.5Y_2O_3$ $5.6Yb_2O_3$ $5.2Gd_2O_3$ TBCs in CMAS: CaO-MgO-Al_2O_3-SiO_2. *J. Aust. Ceram. Soc.* **2021**, *57*, 215–224. [CrossRef]
38. Li, Y.; She, Y.; Liao, K. Hot-Corrosion Behavior of Gd_2O_3–Yb_2O_3 Co-Doped YSZ Thermal Barrier Coatings in the Presence of V_2O_5 Molten Salt. *Coatings* **2023**, *13*, 886. [CrossRef]
39. Wang, T.; Shao, F.; Ni, J.; Zhao, H.; Zhuang, Y.; Sheng, J.; Zhong, X.; Yang, J.; Tao, S.; Yang, K. Calcium-Magnesium-Aluminum-Silicate (CMAS) Corrosion Resistance of Y-Yb-Gd-Stabilized Zirconia Thermal Barrier Coatings. *J. Therm. Spray Tech.* **2021**, *30*, 442–456. [CrossRef]
40. Borom, M.P.; Johnson, C.A.; Peluso, L.A. Role of Environment Deposits and Operating Surface Temperature in Spallation of Air Plasma Sprayed Thermal Barrier Coatings. *Surf. Coat. Technol.* **1996**, *86–87*, 116–126. [CrossRef]
41. Li, D.; Jiang, P.; Gao, R.; Sun, F.; Jin, X.; Fan, X. Experimental and Numerical Investigation on the Thermal and Mechanical Behaviours of Thermal Barrier Coatings Exposed to CMAS Corrosion. *J. Adv. Ceram.* **2021**, *10*, 551–564. [CrossRef]
42. Krämer, S.; Yang, J.; Levi, C.G. Infiltration-Inhibiting Reaction of Gadolinium Zirconate Thermal Barrier Coatings with CMAS Melts. *J. Am. Ceram. Soc.* **2008**, *91*, 576–583. [CrossRef]
43. Krämer, S.; Yang, J.; Levi, C.G.; Johnson, C.A. Thermochemical Interaction of Thermal Barrier Coatings with Molten CaO-MgO-Al_2O_3-SiO_2 (CMAS) Deposits. *J. Am. Ceram. Soc.* **2006**, *89*, 3167–3175. [CrossRef]
44. Guo, L.; Xin, H.; Li, Y.; Yu, Y.; Yan, Z.; Hu, C.; Ye, F. Self-Crystallization Characteristics of Calcium-Magnesium-Alumina- Silicate (CMAS) Glass under Simulated Conditions for Thermal Barrier Coating Applications. *J. Eur. Ceram. Soc.* **2020**, *40*, 5683–5691. [CrossRef]
45. Aygun, A.; Vasiliev, A.L.; Padture, N.P.; Ma, X. Novel Thermal Barrier Coatings That Are Resistant to High-Temperature Attack by Glassy Deposits. *Acta Mater.* **2007**, *55*, 6734–6745. [CrossRef]
46. Turkdogan, E.T. *Physical Chemistry of High Temperature Technology*; Academic Press: New York, NY, USA, 1980; ISBN 978-0-12-704650-1.

47. Chiu, C.; Tseng, S.; Chao, C.; Fan, X.; Cheng, W. Interfacial Stresses of Thermal Barrier Coating with Film Cooling Holes Induced by CMAS Infiltration. *Coatings* **2022**, *12*, 326. [CrossRef]
48. Mohan, P.; Yuan, B.; Patterson, T.; Desai, V.; Sohn, Y.H. Degradation of Yttria Stabilized Zirconia Thermal Barrier Coatings by Molten CMAS (CaO-MgO-Al_2O_3-SiO_2) Deposits. *MSF* **2008**, *595–598*, 207–212. [CrossRef]
49. Ahmed, Q.; Qureshi, I.N.; Salam, I.U. Investigation of Hot Section (Nozzle Guiding Vane) Distress Due to Interaction of Thermal Barrier Coatings with CMAS. *KEM* **2018**, *778*, 245–250. [CrossRef]
50. Wang, J.; Chen, L.; Wang, M.; Zhang, C.; Yu, Y.; Sun, J.; Chen, X.; Wang, Y.; Liu, P.; Jing, Q. Influence of Gd_2O_3 Substitution on Thermal and Mechanical Properties of ZrO_2-Ta_2O_5-Y_2O_3. *J. Eur. Ceram. Soc.* **2021**, *41*, 1654–1663. [CrossRef]
51. Stott, F.H.; de Wet, D.J.; Taylor, R. Degradation of Thermal-Barrier Coatings at Very High Temperatures. *MRS Bull.* **1994**, *19*, 46–49. [CrossRef]
52. Liu, Y.; Cao, Z.; Yuan, J.; Sun, X.; Su, H.; Wang, L. Effect of Morphology, Impact Velocity and Angle of the CaO-MgO-Al_2O_3-SiO_2 (CMAS) Particle on the Erosion Behavior of Thermal Barrier Coatings (TBCs): A Finite Element Simulation Study. *Coatings* **2022**, *12*, 576. [CrossRef]
53. Levi, C.G.; Hutchinson, J.W.; Vidal-Sétif, M.-H.; Johnson, C.A. Environmental Degradation of Thermal-Barrier Coatings by Molten Deposits. *MRS Bull.* **2012**, *37*, 932–941. [CrossRef]
54. Nieto, A.; Agrawal, R.; Bravo, L.; Hofmeister-Mock, C.; Pepi, M.; Ghoshal, A. Calcia–Magnesia–Alumina–Silicate (CMAS) Attack Mechanisms and Roadmap towards Sandphobic Thermal and Environmental Barrier Coatings. *Int. Mater. Rev.* **2021**, *66*, 451–492. [CrossRef]
55. Krause, A.R.; Garces, H.F.; Dwivedi, G.; Ortiz, A.L.; Sampath, S.; Padture, N.P. Calcia-Magnesia-Alumino-Silicate (CMAS)-Induced Degradation and Failure of Air Plasma Sprayed Yttria-Stabilized Zirconia Thermal Barrier Coatings. *Acta Mater.* **2016**, *105*, 355–366. [CrossRef]